ORNL/TM-2023/ 3012

Report on FY 2023 Research and Development on Specially Designed Creep-fatigue Experiments on Alloy 617 in Support of Improving Creep-fatigue Evaluation Approaches

Yanli Wang
Peijun Hou

Approved for public release.
Distribution is unlimited.

August 2023

OAK RIDGE National Laboratory

ORNL IS MANAGED BY UT-BATTELLE LLC FOR THE US DEPARTMENT OF ENERGY

DOCUMENT AVAILABILITY

Reports produced after January 1, 1996, are generally available free via OSTI.GOV.

Website www.osti.gov

Reports produced before January 1, 1996, may be purchased by members of the public from the following source:

National Technical Information Service
5285 Port Royal Road
Springfield, VA 22161
Telephone 703-605-6000 (1-800-553-6847)
TDD 703-487-4639
Fax 703-605-6900
E-mail info@ntis.gov
Website http://classic.ntis.gov/

Reports are available to US Department of Energy (DOE) employees, DOE contractors, Energy Technology Data Exchange representatives, and International Nuclear Information System representatives from the following source:

Office of Scientific and Technical Information
PO Box 62
Oak Ridge, TN 37831
Telephone 865-576-8401
Fax 865-576-5728
E-mail reports@osti.gov
Website https://www.osti.gov/

This report was prepared as an account of work sponsored by an agency of the United States Government. Neither the United States Government nor any agency thereof, nor any of their employees, makes any warranty, express or implied, or assumes any legal liability or responsibility for the accuracy, completeness, or usefulness of any information, apparatus, product, or process disclosed, or represents that its use would not infringe privately owned rights. Reference herein to any specific commercial product, process, or service by trade name, trademark, manufacturer, or otherwise, does not necessarily constitute or imply its endorsement, recommendation, or favoring by the United States Government or any agency thereof. The views and opinions of authors expressed herein do not necessarily state or reflect those of the United States Government or any agency thereof.

ORNL/TM-2023/ 3012

Materials Science and Technology Division

REPORT ON FY 2023 RESEARCH AND DEVELOPMENT ON SPECIALLY DESIGNED CREEP-FATIGUE EXPERIMENTS ON ALLOY 617 IN SUPPORT OF IMPROVING CREEP-FATIGUE EVALUATION APPROACHES

Yanli Wang
Peijun Hou[1]

---

[1] Imtech Corporation, Knoxville

Date Published: August 2023

Prepared by
OAK RIDGE NATIONAL LABORATORY
Oak Ridge, TN 37831
managed by
UT-BATTELLE LLC
for the
US DEPARTMENT OF ENERGY
under contract DE-AC05-00OR22725

CONTENTS

LIST OF FIGURES

LIST OF TABLES

ABBREVIATIONS

ART	Advanced Reactor Technologies
ASME	American Society of Mechanical Engineers
CF	creep-fatigue
DOE	US Department of Energy
EPP	elastic-perfectly plastic
INL	Idaho National Laboratory
ORNL	Oak Ridge National Laboratory
SBSMT	single-bar simplified model test
SMT	simplified model test

ACKNOWLEDGMENTS

This research was sponsored by the US Department of Energy (DOE) under contract no. DE-AC05-00OR22725 with Oak Ridge National Laboratory (ORNL), managed and operated by UT-Battelle LLC. Programmatic direction was provided by the Office of Nuclear Reactor Deployment of the DOE Office of Nuclear Energy (NE).

The authors gratefully acknowledge the support provided by Sue Lesica, DOE-NE Federal Materials Lead for the Advanced Reactor Technologies (ART) Program; Matthew Hahn, DOE-NE Federal Program Manager of the ART Gas-Cooled Reactors (GCR) Campaign; Gerhard Strydom of Idaho National Laboratory, National Technical Director of the ART GCR Campaign; and T.-L. Sham of Idaho National Laboratory, Technology Area Lead, Advanced Materials, ART Program.

The authors thank ORNL staff members Bradley J Hall, C. Shane Hawkins, and Donald L. Erdman for their technical support in carrying out the experiments. The time spent by Lianshan Lin and Zhili Feng of ORNL reviewing this report is acknowledged.

ABSTRACT

Experimental and numerical studies in support of developing the integrated Elastic–Perfectly Plastic (EPP) plus Simplified Model Test (SMT) design methodology, referred to as the EPP+SMT method, continued in FY 2023. This report focuses on the methods for extrapolating the EPP+SMT creep-fatigue life curves at long hold times and low strain ranges at elevated temperatures.

In this work, the available uniaxial creep-fatigue failure data on Alloy 617 at temperatures of 950°C and 850°C were analyzed to provide a guidance on the development of the extrapolation method and the creep-fatigue failure criteria. A viscoplastic constitutive model for Alloy 617 was adopted to extrapolate the mechanical responses to low strain ranges and long hold times. A set of design curves of Alloy 617 at temperatures of 950°C, 850°C, and 800°C with tensile hold times of 1 hr, 100 hr, and 1,000 hr are developed.

Furthermore, creep-fatigue testing on two notch specimen geometries, shallow-notch and sharp V-notch, on Alloy 617 was performed 950°C to understand the multiaxial stress relaxation behavior. The experimental and numerical results on the notch specimens were compared with those on the standard uniaxial smooth bar specimens. The effect of multi-axial stress state combined with elastic follow-up on the stress relaxation behavior was investigated in this report.

1. BACKGROUND

Creep-fatigue (CF) interactive damage is the most damaging mechanism to high temperature structural components under cyclic loading. In the past several decades, researchers in the American Society of Mechanical Engineers (ASME) Boiler and Pressure Vessel Code (BPVC), Section III, Division 5 have devoted to the elevated temperature code rule development to ascertain conservative structural designs against CF failure for high temperature reactors. In general, advances in the CF performance of structural materials are considered to be essential to realize the enhancement in the economics of high temperature reactors. The current Subsection HB, Subpart B CF damage evaluation in the design procedure in BPVC Section III, Division 5 was established based on (1) analytically collecting a detailed time-stress-strain data at elevated temperatures, (2) comparing the stress and strain components with experimental fatigue and CF results, and (3) reassembling the analytical results to form a damage function in a form of the CF damage diagram. The deconstruction and recombination of the stress and strain quantities present difficulties in evaluating experimental data and determining CF damage in design. The uncertainties in these design steps result in a use of the overly conservative approaches in the current CF damage diagram-based design procedure.

The integrated elastic-perfectly plastic (EPP) plus simplified model test (SMT) design methodology, referred to as the EPP+SMT method, is an alternative CF evaluation methodology. This EPP+SMT method aims to maximize the advantages of both EPP methods and the SMT CF evaluation approach and minimize the over-conservatism in the existing CF evaluation procedure while properly accounting for enhanced creep damage around localized defects and stress risers. The key is that it no longer requires the use of the damage interaction, or damage diagram, and the combined effects of creep and fatigue are accounted for in the SMT testing data. The SMT specimens are designed to replicate or bound the stress and strain redistribution that occurs in actual components when loaded in the creep regime. On the other hand, the EPP methods greatly simplify the design evaluation procedure by eliminating the need for stress classification, which is the basis of the current simplified design rules.

A detailed plan was developed and subsequently revised for the development of this EPP+SMT methodology (Wang et al. 2016a, 2016b, 2017a, 2018, 2019; Messner 2018). The development of SMT-based design curves requires experimental data, and the parameters to be considered include elastic follow-up factor, strain range, strain rate, testing temperature, hold time, and primary load. In the original SMT key feature testing methods, the elastic follow-up factor was achieved by sizing the length and area ratios of the driver section to the test section. Achieving the requisite representation of creep damage characteristics via key featured SMT, particularly at very high temperatures, involves specimen configurations that are both costly and beyond the limits of test control and stability (Wang et al. 2013, 2014, 2015, 2016a, 2017b, 2017c). Although key featured SMT testing is crucial in verifying the SMT-based design methodology, it is impractical for use in generating data for SMT-based design curves.

Wang et al. made significant progress in developing SMT experimental techniques (2018, 2019, 2020). In particular, the newly developed single-bar SMT (SBSMT) test method and test protocol overcame many challenges associated with SMT key feature experiments and enabled the evaluation of the elastic follow-up effect by using a standard CF specimen without specialized instrumentation and specimen design. In FY 2019, Wang et al. (2019) demonstrated the SBSMT method on Alloy 617, SS316H, and Grade 91 by testing at high temperatures and successfully showed the flexibility of generating SMT-based failure data with a wide range of elastic follow-up values from 1 to 12. In FY2022, Idaho National Laboratory (INL) applied the SBSMT method using software feedback control (Wang, 2022). The SBSMT test method significantly simplifies the procedure for generating SMT test data and allows SMT-based design method development to advance rapidly.

In FY 2020, Wang et al. (2020, 2021a, 2021b) extended the SBSMT method to internal pressurized tubular specimens at 950°C on Alloy 617. The sustained primary load was introduced by the internal pressure. The test results from this study along with the original SMT data on Alloy 617, demonstrated that although internal pressure is within the allowable stress limit per ASME Section III, Division 5, Code Case N-898, the SMT CF cycles to failure were reduced for the cases tested with primary-pressure load. The reduction of SMT CF life because of primary load was found to be dependent on strain ranges and elastic follow-up factors. Approaches to account for the primary-load effect on SMT design curves were discussed in Barua et al. (2020, 2021), and the results show that the EPP strain range analysis procedure naturally captures the primary pressure effect. Barua et al. (2020, 2021) also demonstrated that the EPP+SMT methodology is much simpler to execute than conventional CF damage analyses through multiple sample problems. The remaining critical factors in finalizing the SMT-based design curves are the methods for extrapolating the design curves to the low strain range region and with longer hold times (such as long hold time of 1,000 h) that are prototypical of plant operations.

In this report, strain-controlled standard CF test data and SMT CF test data are used to calibrate a viscoplastic constitutive model for Alloy 617. The constitutive model was used to extrapolate the mechanical responses to low strain range and long hold time. Finally, a set of design curves of Alloy 617 at temperatures of 950°C, 850°C, and 800°C with long hold times are developed.

Furthermore, in order to probe the key features of high temperature components under cyclic loading, experiments are designed to study multi-axial stress state and its influence on the stress relaxation behavior and CF life cycles. To this end, this study is also aiming to collect multiaxial CF failure data in addition to demonstrate the effect of multiaxial stress relaxation behavior.

2. MATERIAL, EXPERIMENTAL, AND CREEP FATIGUE DATA

2.1 MATERIALS AND SPECIMENS

The commercial hot-rolled Alloy 617 plate (UNS N06617) with heat number 314626 from ThyssenKrupp VDM USA Inc. was used in this study. The nominal thickness of the material plate is 38 mm. Table 1 summarizes the chemical compositions of this nickel-based Alloy 617 material. All the CF specimens in this study were machined from the as-received plate under solution annealed condition.

Table 1. Chemical compositions of the Alloy 617 plate with heat 314626 (wt%)

C	S	Cr	Mn	Si	Mo	Ti	Cu	Fe	Al	Co	B	Ni
0.05	<0.002	22.2	0.1	0.1	8.6	0.4	0.04	1.6	1.1	11.6	<0.001	balance

In the report, the standard uniform specimen geometry in Figure 1 is referred as the smooth bar specimen, and it is under uniaxial stress state during CF loading. The standard specimen has a 19.05 mm gauge length and a 6.35 mm gauge diameter. To generate stress concentration and multiaxial stress state, two types of notch geometries are designed in the gage section. Figure 2 shows the details the shallow-notch and sharp V-notch. In order to simplify the specimen machining procedure, notches were machined on a straight bar with a total length of 177.8 mm and a 12.7 mm diameter. The notch area was mechanically polished. The notch designation followed the ASTM Standard E292-09 (ASTM E292-09, 2009). The ratio of the outer diameter to inner diameter in both shallow-notch and V-notch specimens is approximately $\sqrt{2}$.

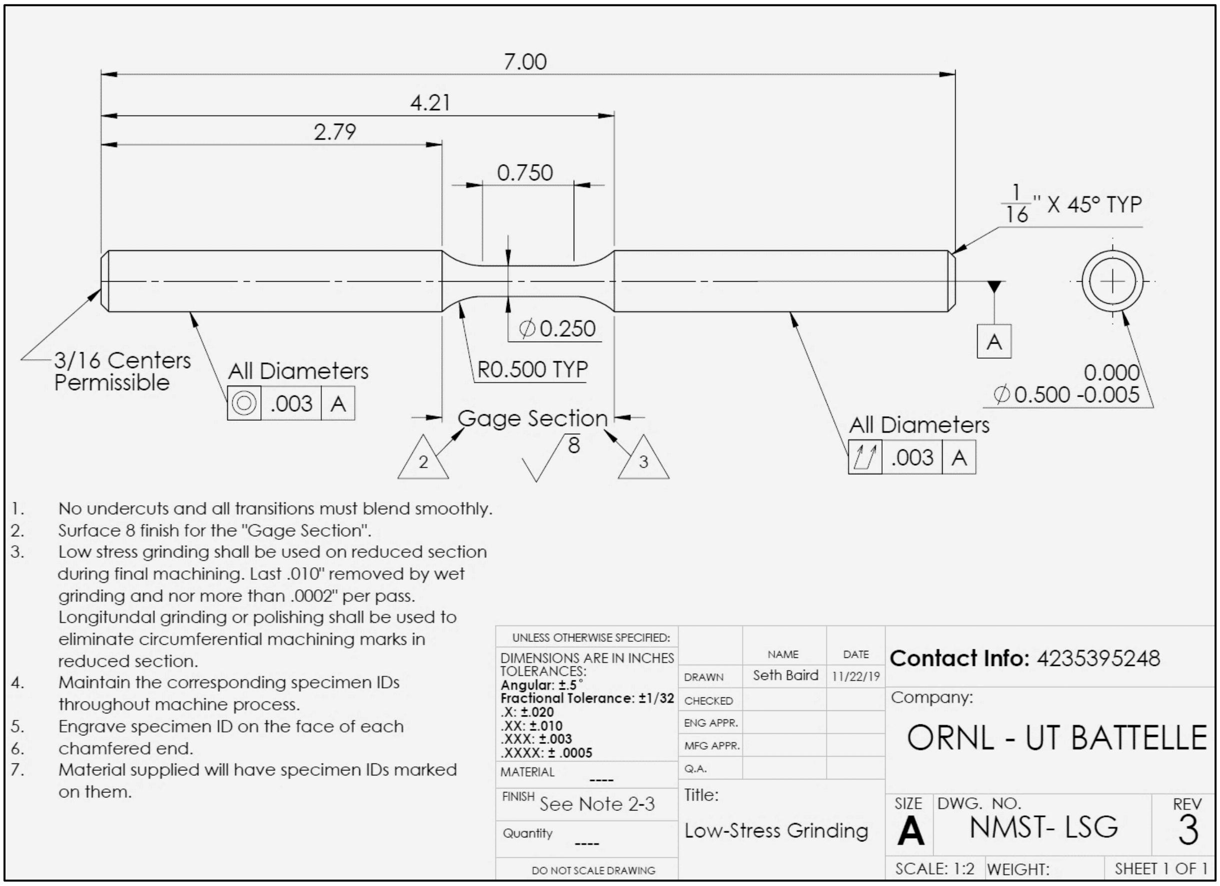

1. No undercuts and all transitions must blend smoothly.
2. Surface 8 finish for the "Gage Section".
3. Low stress grinding shall be used on reduced section during final machining. Last .010" removed by wet grinding and nor more than .0002" per pass. Longitundal grinding or polishing shall be used to eliminate circumferential machining marks in reduced section.
4. Maintain the corresponding specimen IDs throughout machine process.
5. Engrave specimen ID on the face of each
6. chamfered end.
7. Material supplied will have specimen IDs marked on them.

Figure 1. Standard creep-fatigue specimen geometry at Oak Ridge National Laboratory. Dimensions are in inches.

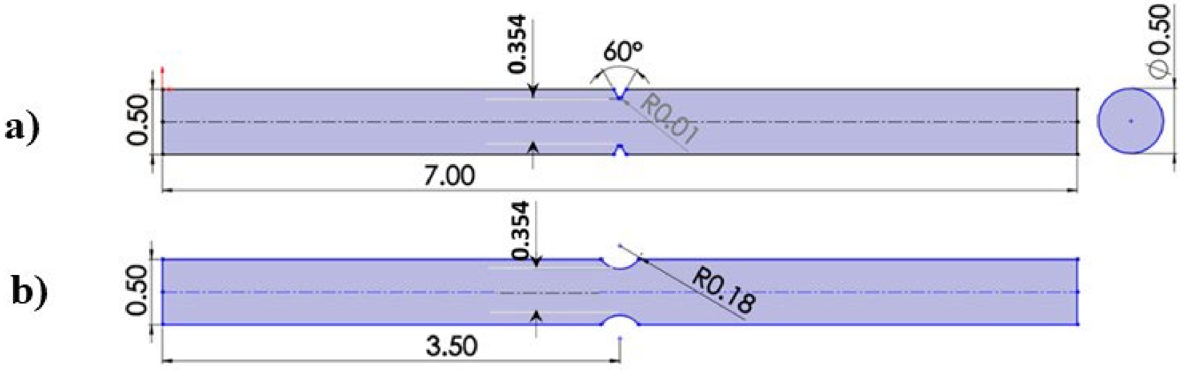

Figure 2. Geometry of creep-fatigue notch specimens with (a) sharp V-notch and (b) shallow-notch. Dimensions are in inches.

2.2 ALLOY 617 CF DATA AND EXPERIMENTS

In support of developing EPP+SMT CF design curves for Alloy 617 at elevated temperatures, uniaxial tensile-hold CF data collected at relatively high strain ranges and short hold times at ORNL and INL are used to perform CF damage evaluation and subsequently to predict the CF life. It should be noted that these available CF testing data were generated on standard uniform smooth bar specimens with testing temperatures of 950 °C and 850 °C. The CF testing procedure followed ASTM E2714-13 (ASTM 2013) and ASTM-E606 (ASTM 2021) standards under strain-controlled mode.

All the experimental CF data were collected using a loading profile, schematically shown in Figure 3. The hold-time period was applied to the maximum tensile strain amplitude, and the loading profile is fully reversed with 1×10^{-3} /s nominal strain rate. The testing conditions and cycles to failure are summarized in Table 2.

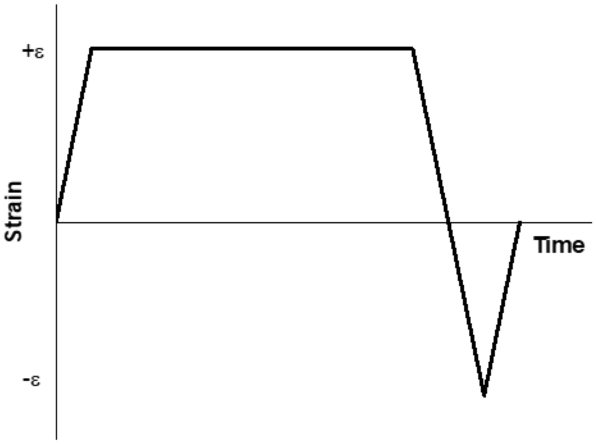

Figure 3. Creep-fatigue loading profile under strain-controlled mode.

Table 2. Creep-fatigue failure data measured at temperature of 950 °C and 850 °C used in this study.

Data source	Specimen ID	Temperature, C	Strain range, %	Tensile hold time, s	Cycle to failure
INL	A-6	950	1.0	180	350
	F-5	950	1.0	180	450
	A-13	950	1.0	600	300
	E-1	950	1.0	600	400
	E-8	950	1.0	600	400
	F-4	950	1.0	600	400
	E-7	950	1.0	1,800	350
	E-9	950	1.0	1,800	350
	E-10	950	1.0	9,000	350
	A-23	950	0.6	180	949
	A-14	950	0.6	600	550
	B-18	950	0.6	600	700
	B-19	950	0.6	600	600
	B-21	950	0.6	1,800	650
	B-5	950	0.3	180	3,899
	B-6	950	0.3	180	2,399
	A-22	950	0.3	600	4,399
	B-7	950	0.3	600	3,999
	B-9	950	0.3	600	2,599
	B-8	950	0.3	1,800	4,599
	B-11	950	0.3	1,800	4,799
	4-2-1	850	1.0	180	502
	4-2-4	850	1.0	180	698
	4-2-2	850	1.0	600	498
	4-2-5	850	1.0	600	502
	4-2-7	850	1.0	1,800	370
	4-2-8	850	1.0	1,800	498
	4-1-10	850	0.3	180	1,902
	4-1-12	850	0.3	180	2,502
	4-1-20	850	0.3	600	1,498
	4-1-22	850	0.3	600	1,798
	4-2-9	850	0.3	600	2,100
	4-7-1	850	0.3	1,800	1,200
	4-7-3	850	0.3	1,800	1,298
ORNL	R13TC6	950	0.17	120	64,659
	*SBA7-P20	950	0.25	600	3,224

Note: * this creep-fatigue test was performed with elastic follow-up factor of 2.

In addition, in order to collect multiaxial CF failure data and to demonstrate the effect of multiaxial stress state on stress relaxation behavior, strain-controlled tensile-hold CF tests were designed and carried out on notch specimens of Alloy 617 at 950 °C. It should be noted that the applied loading profile in these CF tests for notch specimens is globally strain-controlled in the section of nominal gauge length of the extensometer, as illustrated in Figure 4. Table 3 lists the testing conditions for notch specimens conducted at ORNL.

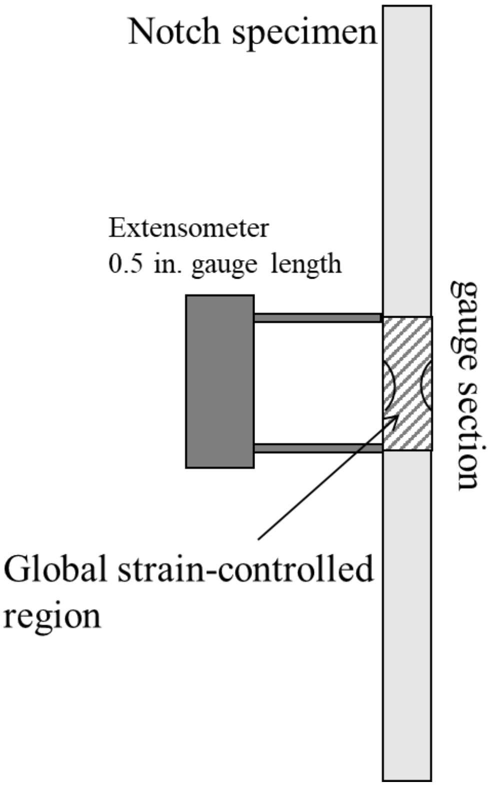

Figure 4. Schematic of the experimental creep-fatigue test setup for notch specimens.

Table 3. Tensile-hold creep-fatigue test conditions on notch specimens for Alloy 617.

Notch specimen	Temperature, °C	Nominal strain range applied to the gage section, %	Tensile hold time, s
Shallow-notch	950	0.6	600
Shallow-notch	950	0.6	3,600
V-notch	950	0.6	600
V-notch	950	0.6	3,600

3. DAMAGE ANALYSIS METHODOLOGY AND NUMERICAL MODEL

3.1 ENERGY-BASED DAMAGE EVALUATION METHOD

In our recent study (Hou, P et al. 2023a), it was concluded that the time fraction-based method was overly conservative and energy-based method is more practical on CF prediction at elevated temperature. In this study, the accumulated damage during CF deformation is assessed using the energy-based method as a failure prediction model (Hou, P et al. 2023a). The energy-based damage evaluation method is briefly outlined below.

The energy-based damage at cycle *i*, w^i, is defined by the strain energy density at cycle *i*, in Eq. 1:

$$w^i = \int \sigma d\epsilon \qquad (1)$$

where σ is the stress and ϵ is the strain. And the strain energy density accumulated at cycle N, w, is given by:

$$w = \sum_{1}^{N} w^i \tag{2}$$

where w^i is the strain energy density at cycle i.

Definitions of strain energy density in the stress-strain hysteresis loops are illustrated in Figure 5. Figure 5a shows the strain energy density at one hysteresis loop at relatively high strain range, w^{I}, as the purple region, which also includes the tensile creep strain energy density caused by the hold marked as the shadowed area. Figure 5b shows the schematic of stress-strain curves at very low strain range for the first and second cycles, where the hysteresis loop almost diminishes for the second cycle. In such case, the accumulated strain energy density (i.e., CF damage) represented by the purple area equals to the accumulated creep strain energy density. When the strain range becomes too low to show a hysteresis loops in the stress-strain curves, there should be a maximum limit in the total accumulated strain energy density when the relaxation stresses reach to zero during the hold.

In this study, the accumulated strain energy density, w, is calculated for each cycle and the failure strain energy density, w_f, is determined through evaluating the standard and SMT-based CF failure data.

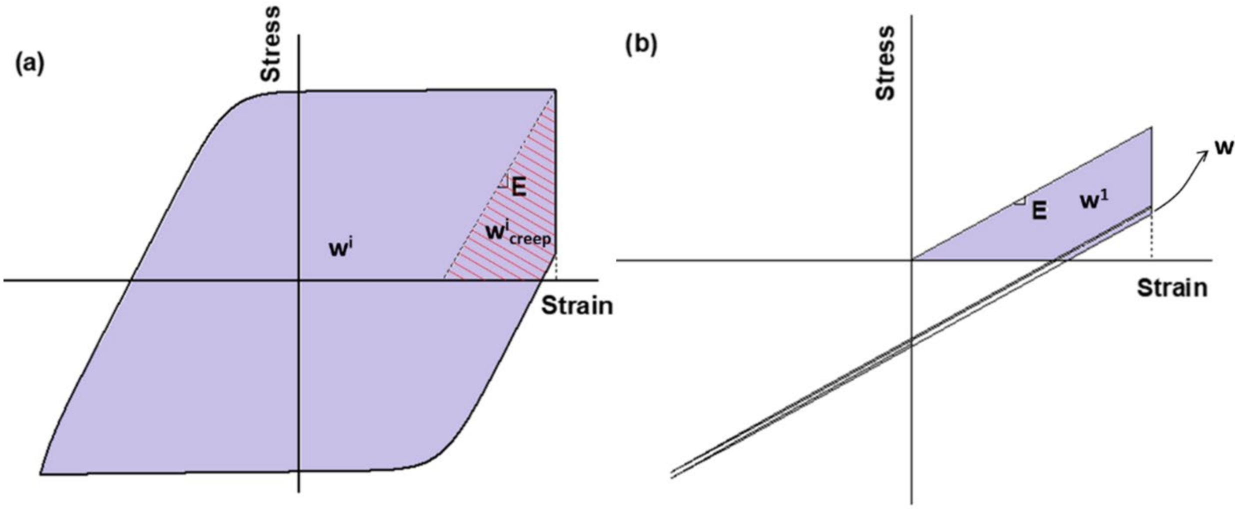

Figure 5. Schematics of the definitions of strain energy density in a stress-strain hysteresis loop at (a) relatively high strain range and (b) low strain range under creep-fatigue loading.

3.2 UNIFIED VISCOPLASTIC CONSTITUTIVE MODEL

A unified viscoplastic constitutive model used in this study to describe the mechanical responses of Alloy 617 at elevated temperatures is briefly outlined in this section (Messner, M.C. 2022 and Messner, M.C. et al. 2021). It is noted that the model is re-calibrated with experimental data to better describe the material behavior at the interested temperatures for this study.

This material model is governed by a time integration of the strain rate decomposition, that is given by:

$$\dot{\boldsymbol{\epsilon}} = \dot{\boldsymbol{\epsilon}}_{\boldsymbol{e}} + \dot{\boldsymbol{\epsilon}}_{\boldsymbol{in}} + \dot{\boldsymbol{\epsilon}}_{\boldsymbol{th}} \tag{3}$$

with

$$\dot{\boldsymbol{\epsilon}}_{\boldsymbol{e}} = \mathbf{C}^{-1} : \dot{\boldsymbol{\sigma}} \tag{4}$$

$$\dot{\boldsymbol{\epsilon}}_{\boldsymbol{th}} = \alpha \dot{T} \mathbf{I} \tag{5}$$

where $\dot{\boldsymbol{\epsilon}}_{\boldsymbol{e}}$ is the elastic strain rate tensor, $\dot{\boldsymbol{\epsilon}}_{\boldsymbol{in}}$ is the inelastic strain rate tensor, $\dot{\boldsymbol{\epsilon}}_{\boldsymbol{th}}$ is the thermal strain rate tensor, $\mathbf{C}$ is the isotropic elasticity tensor calculated using the temperature-dependent elastic modulus and Poisson's ratio, α is the thermal expansion coefficient, and $\mathbf{I}$ is the identity tensor.

Eq. 4 is implemented as a numerical integration for the stress as:

$$\dot{\boldsymbol{\sigma}} = \mathbf{C} : (\dot{\boldsymbol{\epsilon}} - \dot{\boldsymbol{\epsilon}}_{\boldsymbol{in}} - \dot{\boldsymbol{\epsilon}}_{\boldsymbol{th}}) \tag{6}$$

where $\dot{\boldsymbol{\sigma}}$ is the stress rate tensor. The inelastic strain rate is given by:

$$\dot{\boldsymbol{\epsilon}}_{\boldsymbol{in}} = \dot{\gamma} \frac{\partial f}{\partial \boldsymbol{\sigma}} \tag{7}$$

where $\dot{\gamma}$ is the consistency parameter, and f is the yield function, which is given by:

$$f = \sqrt{\frac{3}{2}(\mathbf{s} - \mathbf{x}) : (\mathbf{s} - \mathbf{x})} - \sqrt{\frac{2}{3}}(\sigma_0 + \sigma_R) \tag{8}$$

where $\mathbf{s}$ is the deviatoric stress tensor, $\mathbf{x}$ is the back stress tensor, σ_0 is the rate-independent threshold stress, and σ_R is the isotropic hardening deformation resistance. Those terms in Eq. 8 are given by the following equations:

$$\mathbf{s} = \boldsymbol{\sigma} - \frac{1}{3}\mathrm{tr}(\boldsymbol{\sigma})\mathbf{I} \tag{9}$$

$$\mathbf{x} = \sum_{i}^{3} \mathbf{x}_i \tag{10}$$

$$\dot{\mathbf{x}}_i = \left(\frac{2}{3} C_i \frac{\partial f}{\partial \boldsymbol{\sigma}} - \sqrt{\frac{2}{3}} \gamma_i \mathbf{x}_i \right) \dot{\gamma} \tag{11}$$

$$\dot{\sigma}_R = \delta(Q - \sigma_R)\dot{\gamma} \tag{12}$$

$$\sigma_0 = \mu e^{C_{km}} \tag{13}$$

where $\mathbf{x}_i$ is the back stress component tensor, $\dot{\mathbf{x}}_i$ is the back stress component rate tensor, C_i is the back stress component hardening rate, γ_i is the back stress component, and $\dot{\gamma}$ is the back stress component dynamic recovery rate, $\dot{\sigma}_R$ is the isotropic hardening rate, δ and Q are the temperature-dependent isotropic hardening parameters, and μ is shear modulus, given by:

$$\mu = \frac{E}{2(1 + \nu)} \tag{14}$$

Based on the Kocks-Mecking diagram, the material model switches from a rate sensitive response mode to an insensitive response mode as the temperature and/or strain rate changes. In this model, the inelastic strain rate sensitivity is controlled by the Kocks-Mecking normalized activation energy, g, given as:

$$g = \frac{k(T + 273.15)}{\mu b^3} \log \frac{\dot{\epsilon}_0}{\sqrt{\frac{2}{3}\epsilon_{ij}\epsilon_{ij}}} \tag{15}$$

where k is the Boltzmann constant, μ is the shear modulus, b is the Burgers vector, and $\dot{\epsilon}_0$ is a reference strain rate. g_0 is defined as the critical normalized activation energy which identifies the rate-dependent regime and the rate-independent regime. When $g \leq g_0$, the model is rate-independent, and consistency parameter is given by those conditions as:

$$\dot{\gamma} \geq 0 \tag{16}$$

$$f(\boldsymbol{\sigma}) \leq 0 \tag{17}$$

$$\dot{\gamma} f(\boldsymbol{\sigma}) = 0 \tag{18}$$

$$\dot{\gamma} \dot{f}(\boldsymbol{\sigma}) = 0 \tag{19}$$

When $g > g_0$, the model is rate-dependent, and the consistency parameter is given by the power-law viscoplastic theory defined as:

$$\dot{\gamma} = \sqrt{\frac{3}{2}} \langle \frac{f(\boldsymbol{\sigma})}{\sqrt{\frac{2}{3}}\eta} \rangle^n \tag{20}$$

$$\sigma_0 = 0 \tag{21}$$

where C_{km} is the Kocks-Mecking horizontal asymptote, n and η are material parameters which depend on temperature, and $\langle \ldots \rangle$ denotes the Macaulay brackets.

All the material parameters at temperatures of 950°C and 850°C used in this study are obtained based on experimental CF data (Wright, 2021) and the report by Messner, M.C. (2022). These parameters are listed in Table 4.

Although the predictive capability for the CF mechanical responses of the numerical model could be adopted to lower temperatures in theory, computational model prediction is challenging at these temperatures due to the absence of experimental CF data at corresponding temperatures of interest. To this end, to further predict CF life at 800°C, the isochronous curves in Alloy 617 Code Case N-898 were used to estimate stress relaxation curves, which were further applied to calibrate temperature-dependent material parameters of model. The creep strain rate from isochronous curves is given by:

$$\dot{\varepsilon}_c = \dot{\varepsilon}_{iso} \exp\left(\frac{B_2 \mu {b_{iso}}^3}{AkT_k}\right) \cdot \left(\frac{\sigma}{\mu}\right)^{-\mu {b_{iso}}^3 / AkT_k} \tag{22}$$

where $\dot{\varepsilon}_{iso}$ is reference strain rate, b_{iso} is Burger's vector, A and B_2 are material parameters, μ is shear modulus, and T_k is absolute temperature. Table 4 also listed the model parameters calibrated based on isochronous curve at 800°C and parameters in Eq. 22 describing creep strain rate.

Table 4. Material parameters used in the unified viscoplastic constitutive model.

	Parameter	Symbol	Value	Unit
Numerical model				
	Elastic modulus at 950°C	E	136,000	MPa
	Elastic modulus at 850°C	E	146,000	MPa
	Elastic modulus at 800°C	E	152,000	MPa
	Poisson's ratio	υ	0.31	-
	Boltzmann constant	k	1.38064×10^{-20}	mJ//°C
	Burger's vector	b	2.747×10^{-7}	mm
	Reference strain rate	$\dot{\epsilon}_0$	1.0×10^{10}	/s
	Material parameter 1 at 950°C	n	5.83	-
	Material parameter 1 at 850°C	n	7.40	-
	*Material parameter 1 at 800°C	n	8.80	-
	Material parameter 2 at 950°C	η	511.6	-
	Material parameter 2 at 850°C	η	467.5	-
	*Material parameter 1 at 800°C	η	515.0	-
	KM horizontal asymptote	C_{km}	-5.550	-
	KM intersection point	g_0	0.6112	-
	Back stress 1 hardening rate	C_1	643.9330	Mpa
	Back stress 2 hardening rate	C_2	40.3267	Mpa
	Back stress 3 hardening rate	C_3	-20.6000	Mpa
	Dynamic recovery rate 1	γ_1	103.700	-
	Dynamic recovery rate 2	γ_2	5.089	-
	Dynamic recovery rate 3	γ_3	0.9823	-
	Isotropic strain hardening	Q	-17.73	-
	Isotropic strain hardening	δ	10.32	-
Isochronous curve*				
	Reference strain rate	$\dot{\varepsilon}_{iso}$	5.961×10^{10}	/s
	Burger's vector	b_{iso}	2.019×10^{-7}	mm
	Material parameter 1	A	-4.480	-
	Material parameter 2	B_2	-3.174	-

Note: * material parameters in material model were calibrated based on isochronous curves.

4. CREEP-FATIGUE LIFE PREDICTION

4.1 CREEP-FATIGUE DAMAGE EVALUATION USING ENERGY-BASED METHOD

Figure 6 show the accumulated damage, i.e., accumulated strain energy density during CF deformation, evaluated using CF test data at 950°C as a function of applied CF cycles. The accumulated damage almost linearly increases as the applied cycle in the log-log scale plot. The damage evolution curves at various tensile hold time, in Figure 6a-c, are quite comparable, indicating that the influence of relatively short tensile hold time on damage accumulation and CF life is insignificant, i.e., a saturated CF failure life for relatively short hold times on the Alloy 617 material at 950°C. This observation is consistent with relevant studies on the tensile-hold CF tests on other high temperature materials.

The damage evolution analysis on the test data at 850°C was not performed in this study due to insufficient cycles recorded in those tests. The accumulated damage 850°C was estimated by multiplying the strain energy density at mid-life cycle by the number of cycles to failure. Figure 6d presents the corresponding accumulated damage at CF failure at 950°C and 850°C for all the available data collected. It shows slightly overlapping trends between two different temperatures. These results show a similar value range in accumulated damage from about 500 mJ/mm^3 to 3,000 mJ/mm^3 for these CF tests at these two temperatures.

In this study, we assume that the minimum value of the total accumulated damage at failure among all the available CF test data is the critical value for CF failure life prediction, i.e., 560 mJ/mm^3 and 506 mJ/mm^3 are used as the critical values in predicting the CF life at temperatures of 950°C and 850°C, respectively. In addition, because of the absence of CF failure data at 800°C, 506 mJ/mm^3 is adopted for CF life prediction at this temperature.

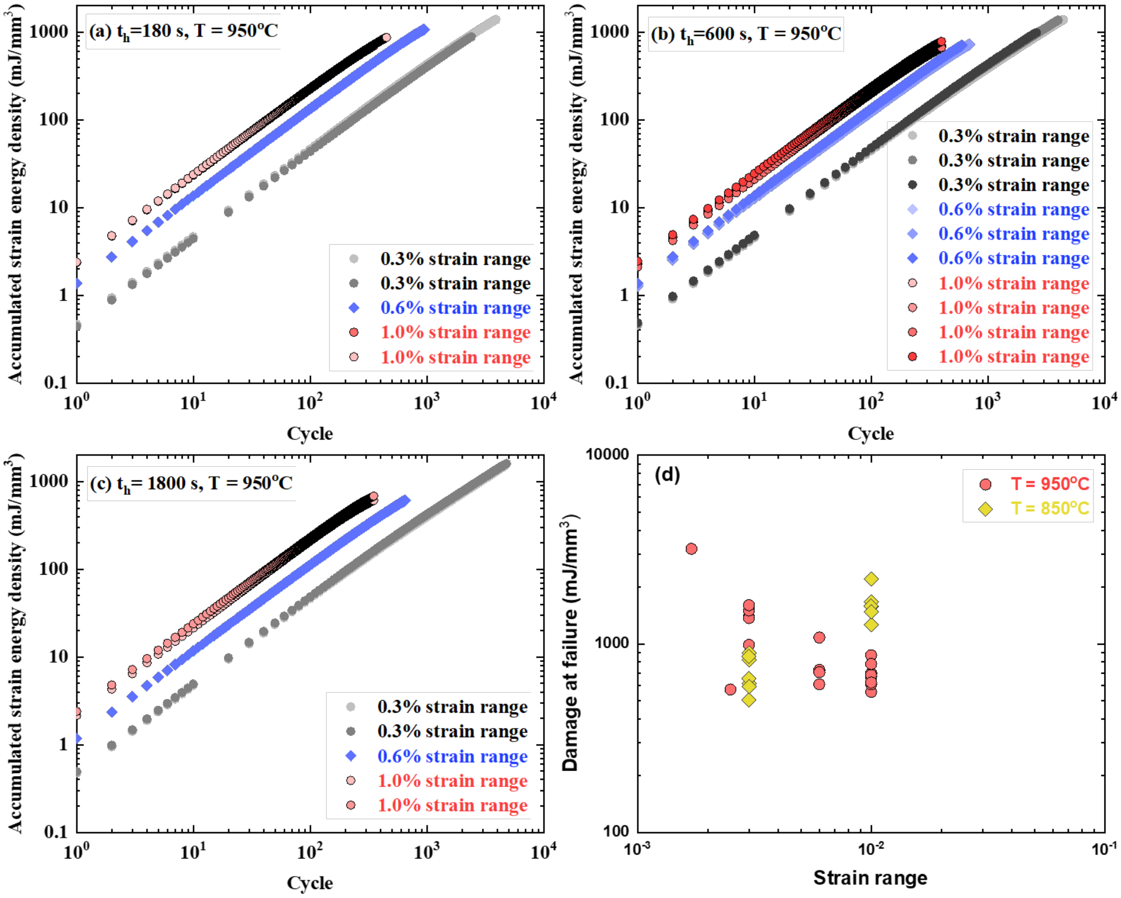

Figure 6. Evolution of the accumulated strain energy density calculated from CF tests with different strain ranges and tensile hold times at 950°C (a, b, c) and (d) the total accumulated strain energy density at cycles to failure at 950°C and 850°C with tensile hold time from 120 s to 9,000 s.

It should be noted that, as illustrated in Figure 5, the accumulated damage has a limit in strain energy density at very low strain range due to the disappearance of the stress-strain hysteresis loops. That is, the calculated accumulated damage would not reach to the minimum value required for material failure, and therefore,

4.2 EXTRAPOLATION METHOD AT 950°C AND 850°C

Unified viscoplastic model simulation was conducted to provide numerical data for extrapolation of accumulated damage to unknown regions, i.e., at long hold times and/or at low strain ranges. It is noted that the material constitutive model parameters are re-calibrated in this study to allow more accurate description of the CF deformation behavior for Alloy 617, as explained in Section 3.

As demonstrated through the above analysis, the experimental results at temperatures of 950°C and 850°C show that the mechanical responses become stable after about 20 cycles, therefore, the accumulated damage of the initial 20 cycles was used for extrapolation on a log-log scale trend line to predict the damage evolution. Figure 7 shows examples of comparison between experimental and numerical CF results at temperature of 850°C. Figure 8 shows examples of numerical results at 0.6% and 0.08% strain ranges at temperature of 950°C with 1 hr and 100 hr tensile hold times. The numerical results at 950°C shows that the accumulated damage increases with the increase of hold time at strain range of 0.6%, in Figure 8a, although the increase is not significant. On the other hand, there is no visible hysteresis loop at strain range of 0.08% with 1 hr tensile hold time, although as tensile hold time increases to 100 hr, the hysteresis loop is present. This observation indicates that the hysteresis loop is influenced by the strain level as well as the hold time.

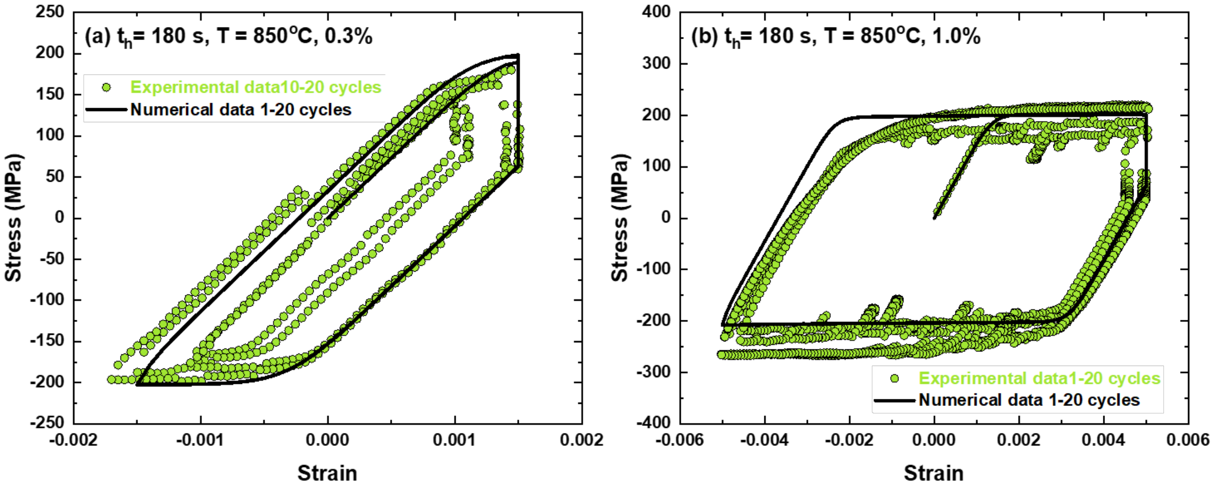

Figure 7. Comparison between experimental and numerical creep-fatigue results at temperature of 850°C. (a) at 0.3% strain range with 180 s tensile hold time. (b) at 1.0% strain range with 180 s tensile hold time.

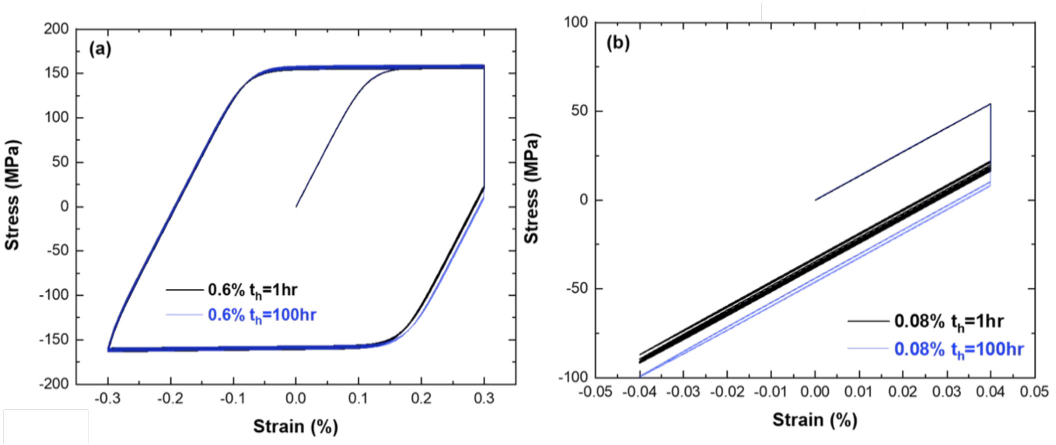

Figure 8. Numerical results at strain ranges of (a) 0.6% and (b) 0.08% and at tensile hold times of 1 hr and 100 hr, the stress-strain curves of initial 20 applied cycles at temperature of 950℃.

Figure 9 illustrates the extrapolation method for extending damage to low strain range and long hold time based on the linear log-log relation between the accumulated damage and applied cycles. The results are presented for the accumulated damage of 0.6% strain range with 1 hr and 100 hr hold times, and 0.08% strain range with 100 hr hold time evaluated based on numerical results at temperature of 950℃. As described above, at low strain range of 0.08%, the accumulated damage cannot reach the cutoff value determining material failure due to the hysteresis loop does not exhibit during deformation.

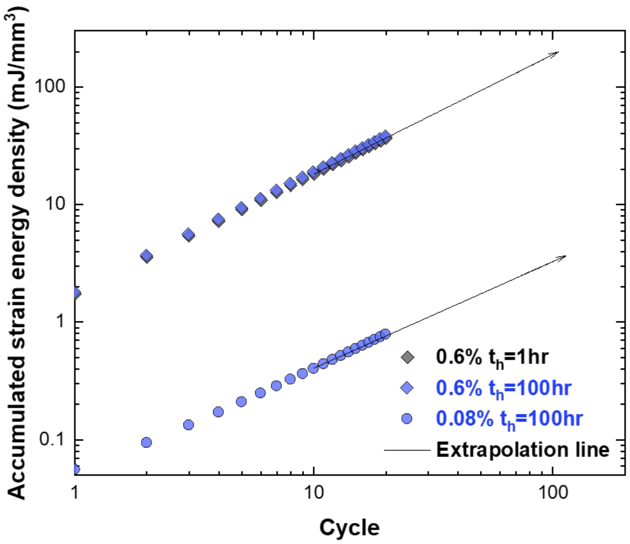

Figure 9. Numerical results of the accumulated CF damage for conditions of 0.6% 1hr, 0.6% 100 hr, and 0.08% 100 hr at temperature of 950℃, along with the schematic extrapolating lines.

4.3 EXTRAPOLATION METHOD AT 800℃ AND LOWER TEMPERAUTRES

As explained in Section 3 of this report, although the predictive capability for the CF mechanical responses of the numerical model could be adopted to lower temperatures in theory, computational model prediction is challenging due to the absence of experimental CF data at temperatures below 850 ℃. For

Alloy 617, stress relaxation due to creep under strain-controlled mode at temperatures higher than 1100 °F (593°C) is expected, as evidently shown from the isochronous curves in the Alloy 617 Code Case N-898.

To predict CF life at 800°C, the average isochronous curves in Alloy 617 Code Case N-898 were used to estimate stress relaxation curves, which were further applied to calibrate temperature-dependent material parameters of model. This comparison allowed us to calibrate temperature-dependent parameters in viscoplastic model at 800°C in the case of lack of experimental CF failure information. Figure 10 shows comparison of stress relaxation curve at hold time of 600 s at temperature of 800°C from between isochronous curves and numerical model.

However, it should be noted that the isochronous curves are established from creep rupture data, and the differences in the mechanical responses of Alloy 617 between constant-stress creep loading and constant-strain creep-fatigue holding are not distinguished in this approach. It is recommended that the material constitutive model should be calibrated to strain-controlled CF experimental data to better describe its CF responses when experimental data become available.

Work on the extrapolation method and CF life curves at lower temperatures between 1100 °F (593°C) and 800°C is beyond the scope of this report.

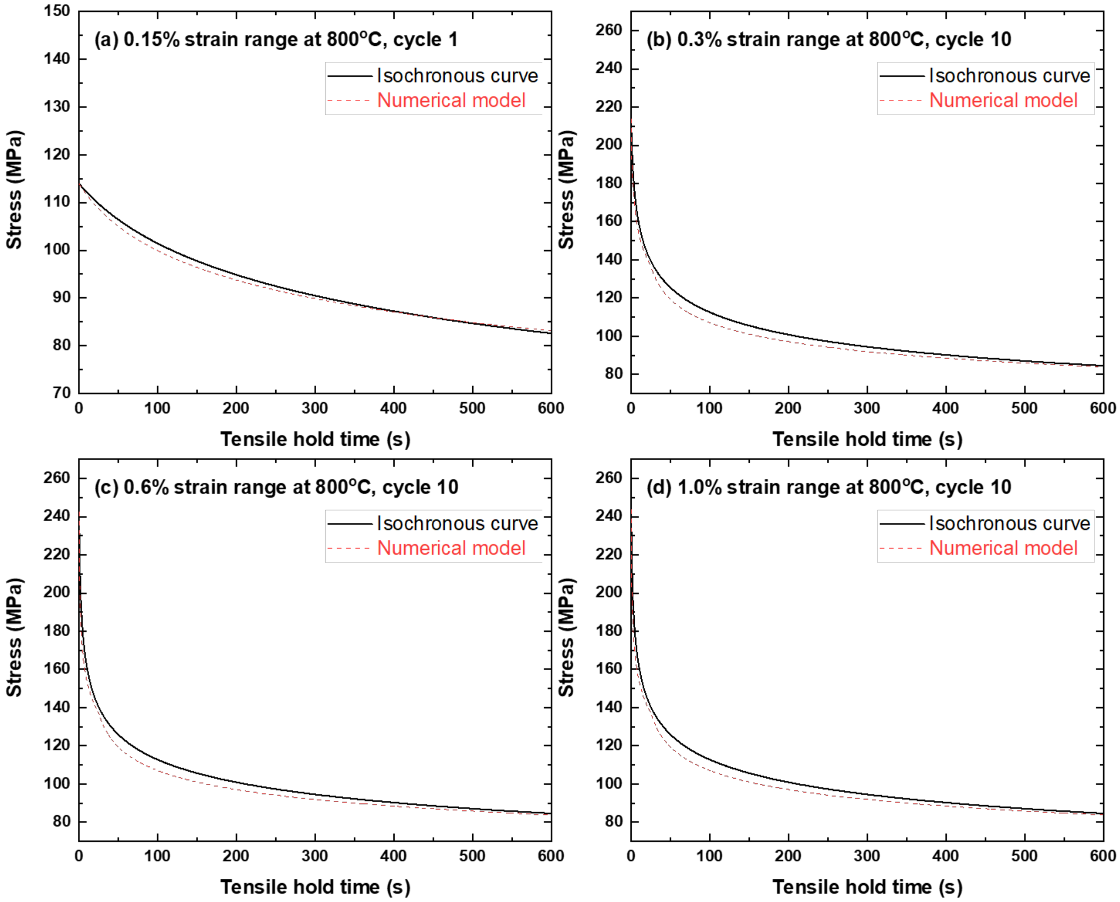

Figure 10. Comparison of stress relaxation curve at hold time of 600 s at temperature of 800°C between the isochronous curves and numerical model. (a) at 0.15% strain range at cycle 1; (b) at 0.3% strain range at cycle 10; (c) at 0.6% strain range at cycle 10; (d) at 1.0% strain range at cycle 10.

4.4 ALLOY 617 CREEP-FATIGUE DESIGN CURVES

The numerical results were used to predict Alloy 617 CF life and extrapolate to low strain ranges and long hold times based on energy-based damage evaluation method. Figure 11 presents the uniaxial CF curves of 1 hr, 100 hr, and 1,000 hr tensile hold times for Alloy 617 at temperatures of 950°C, 850°C, and 800°C, together with CF experimental data points. The pure-fatigue (PF) data and the PF best fit curves are included in the plots for reference. The preliminary CF design curves are established using a conventional approach, i.e., the design curves are determined as the lesser of two curves when a reduction factor of 2 on the strain and a reduction factor of 20 on the cycles to failure are applied to the best-fit CF life curve.

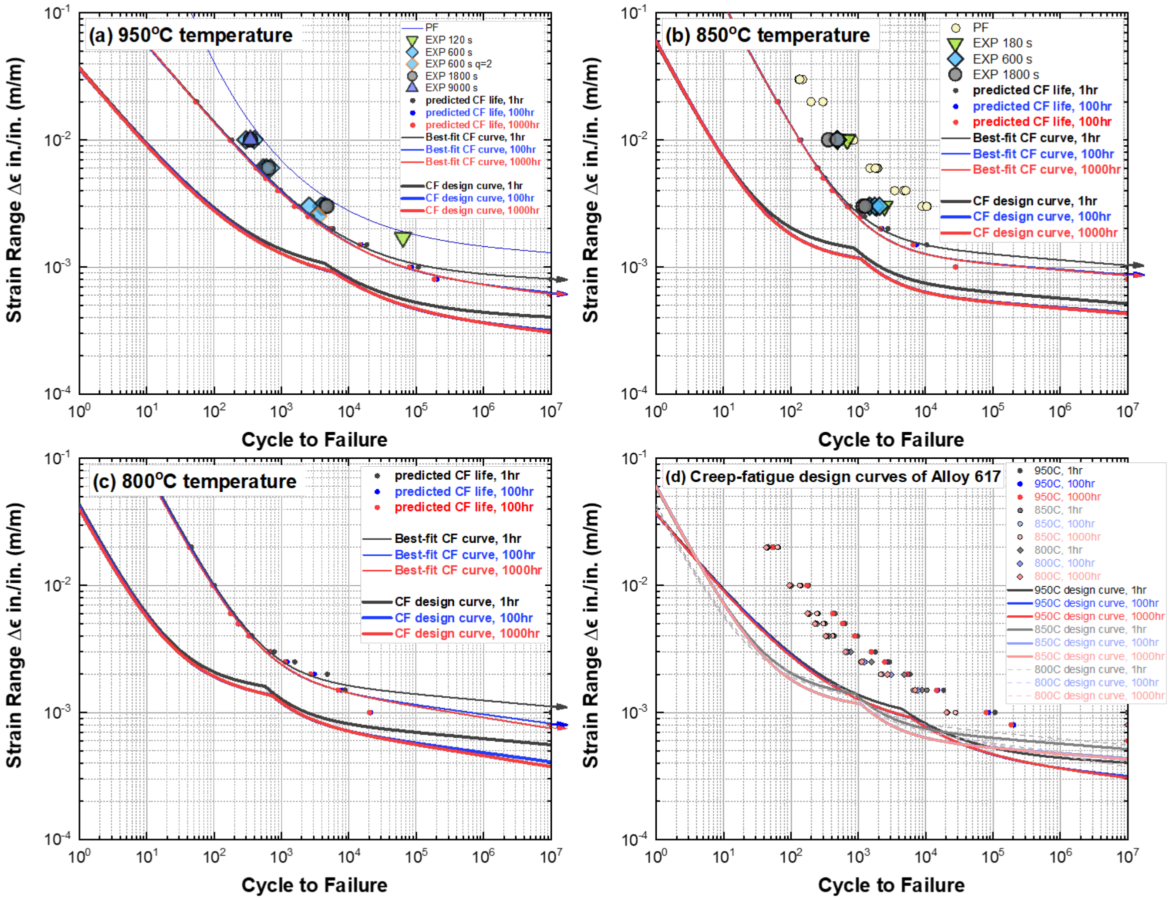

Figure 11. Preliminary tensile-hold creep-fatigue design curves for alloy 617 at temperatures of (a) 950°C, (b) 850°C, and (c) 800°C using energy-based method with elastic follow up factor of 1.0, and (d) the comparison of preliminary tensile-hold creep-fatigue design curves.

5. NOTCH EFFECT ON CREEP-FATIGUE BEHAVIOR OF ALLOY 617 AT ELEVATED TEMPERATURE

5.1 EXPERIMETAL RESULTS

Creep-fatigue experiments on the two types of notch specimens shown in Figure 2 were performed on Alloy 617 at 950 ºC (Hou, P et al, 2023b). Figure 12 shows the maximum, minimum, and relaxation stresses of notch specimens and uniform standard specimens at nominal strain range of 0.6% with 600 s tensile hold time. The stresses in notch specimens were calculated at the cross-sectional area of the uniform section with a diameter of 0.5 in. In another words, the test articles are viewed as part of a component under displacement controlled cyclic axial loading, however this structure geometrically has a severe local area reduction of ~50% caused by the notch.

The comparison of the maximum and minimum stresses for notch and uniform specimens, Figure 12a, shows lower average global axial stresses in notch specimens. The V-notch specimen exhibits higher global axial maximum stresses at initial cycles in comparison to shallow-notch specimen, while V-notch specimen exhibits a continuous decrease in the maximum stresses as the applied cycle increases in comparison to the nearly constant maximum stresses in shallow-notch specimen prior to the failure initiation. In Figure 12b, notch specimens exhibit similar relaxation stresses at the end of the tensile hold of 600 s as uniform specimens. The difference in the average global axial relaxation stresses between V-notch and shallow-notch specimens is not significant. Figure 13 shows the comparison of global stress vs. nominal strain hysteresis loops and stress relaxation curves of the cycle 10 between notch specimens and uniform smooth bar specimens. In addition, the stress-relaxation curves in the notch specimens and smooth bar specimen are normalized by initial stress during hold time stage and the results are presented in Figure 13c. The relaxation stresses and the relaxation behavior during hold are comparable between notch and uniform specimens and the normalized relaxation stresses stayed almost same among uniform and notch specimens.

Figure 14 shows the comparison of the average global maximum and minimum, and the relaxation stresses of V-notch specimen between 600 s and 3,600 s tensile hold time. The maximum and minimum stresses in V-notch specimen with the hold time of 3,600 s are similar to that of 600 s at initial cycles, while they decrease faster in the case of 3,600 s with the increase of applied cycle. The V-notch specimen with 3,600 s hold, in Figure 14b, shows slightly lower relaxation stresses at the end of the hold due to longer hold time. Figure 15 shows the comparison of average global stress vs. nominal strain hysteresis loops and stress relaxation curves of the cycle 10 in V-notch specimens with 600 s and 3,600 s hold, and the results do not show significant differences between these two tests. Similarly, comparisons of the maximum, the minimum, the relaxation stresses, the average global stress vs. nominal strain hysteresis loops of the 10th cycle, and the stress relaxation curves of the 10th cycle of shallow-notch specimens between 600 s and 3,600 s tensile hold time are presented in Figure 16 and Figure 17. The observations in the comparison of shallow-notch specimen are similar to that of V-notch specimen.

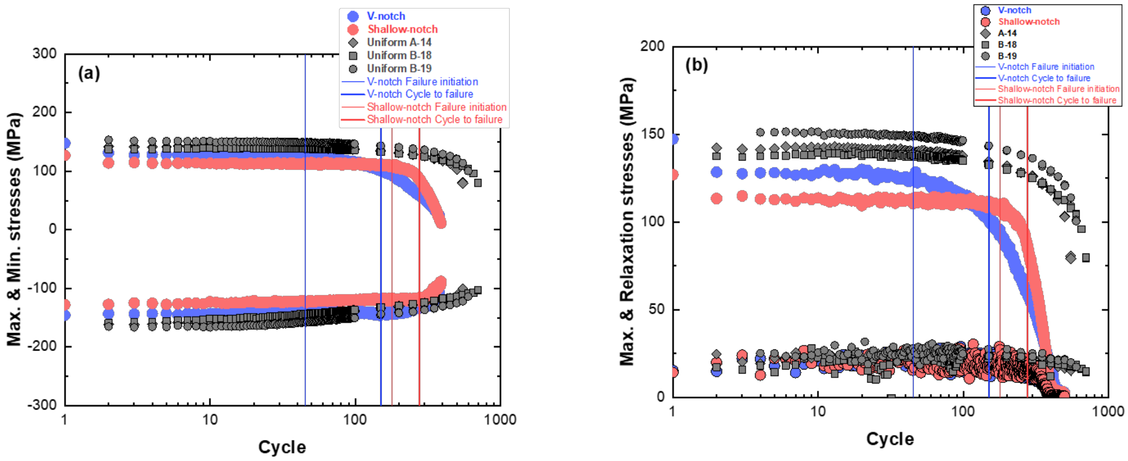

Figure 12. Average global axial maximum, minimum, and relaxation stresses of notch specimens and uniform specimens tested at nominal strain range of 0.6% with 600 s tensile hold time at temperature of 950°C.

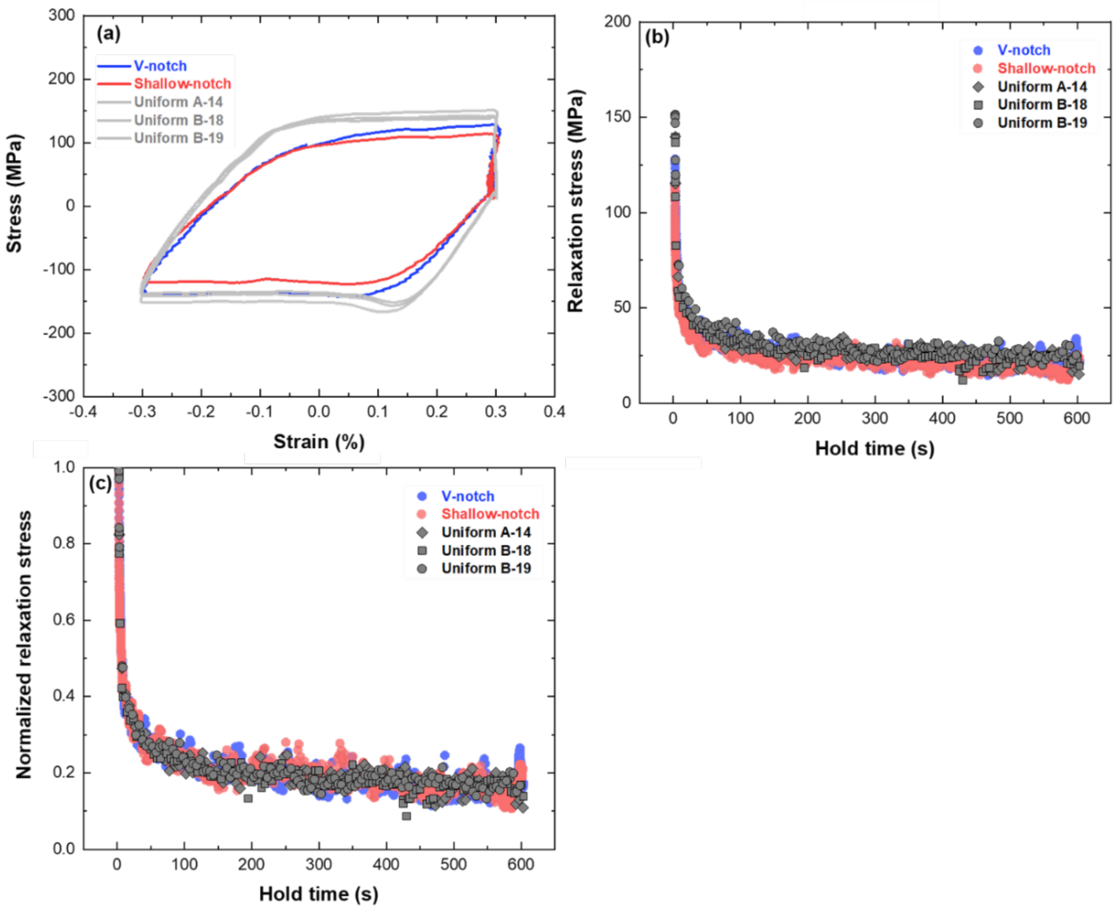

Figure 13. Comparison of the average global axial stress vs. nominal strain hysteresis loops (a), stress relaxation curves (b), and normalized stress relaxation curves (c) of the cycle 10 of the notch specimens and uniform specimens at 950°C.

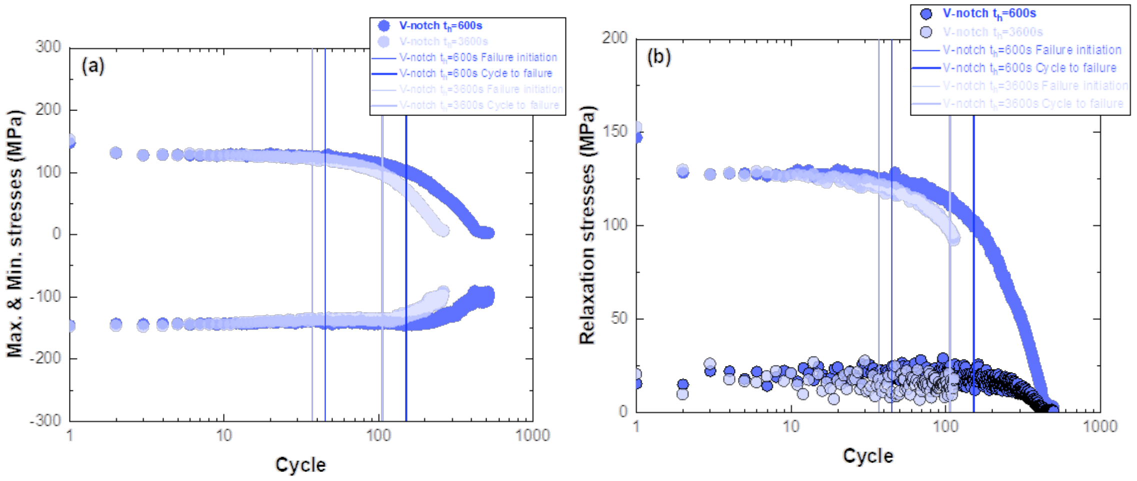

Figure 14. Comparison of the average global maximum and minimum, and the relaxation stresses of V-notch specimen between 600 s and 3600 s tensile hold time at 950°C.

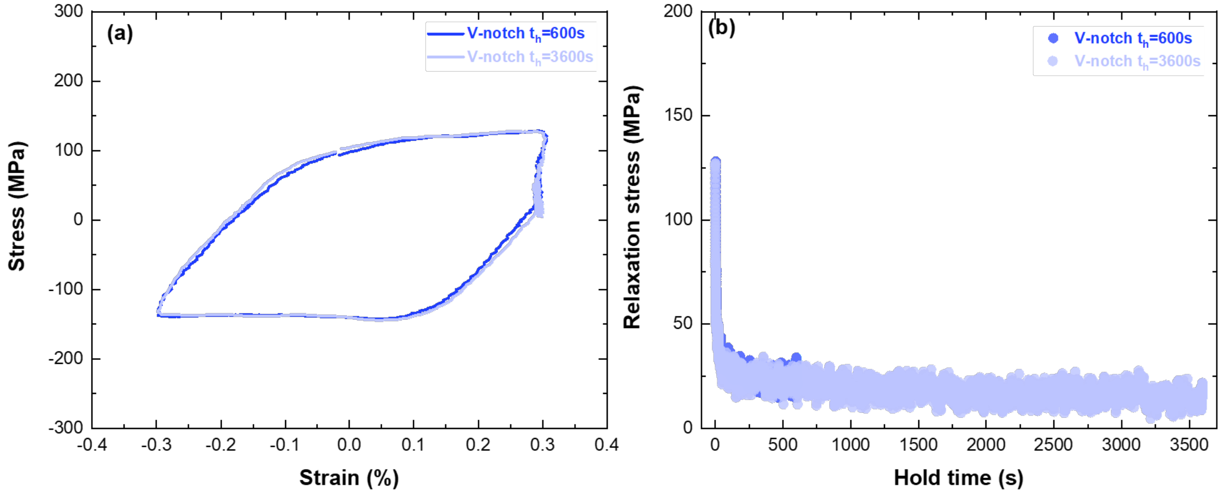

Figure 15. Comparison of average global stress vs nominal strain hysteresis loops and average global stress relaxation curves of the cycle 10 in V-notch specimens with 600 s and 3600 s hold time at 950°C.

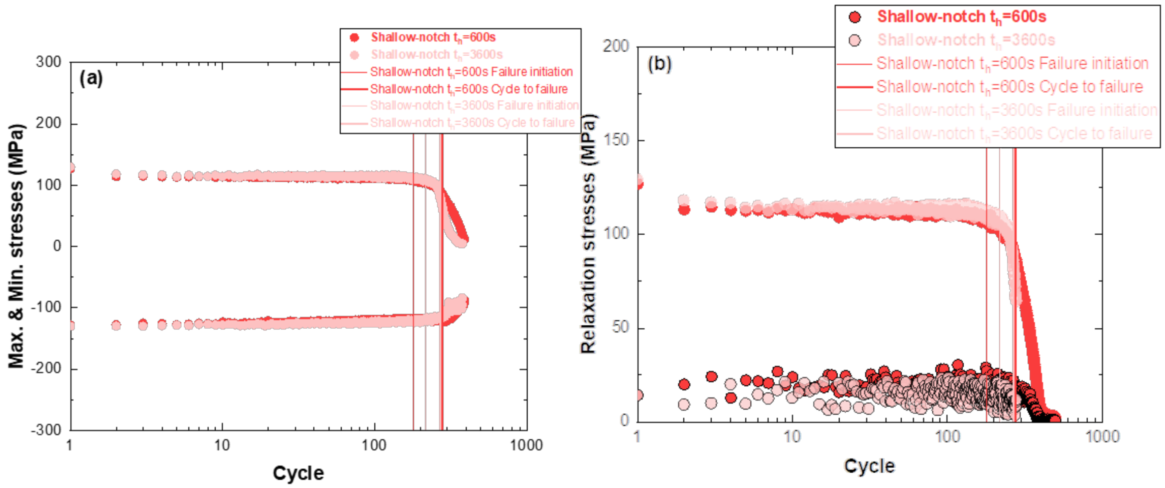

Figure 16. Comparison of the average global maximum and minimum, and the relaxation stresses of shallow-notch specimen between 600 s and 3600 s tensile hold time at 950°C.

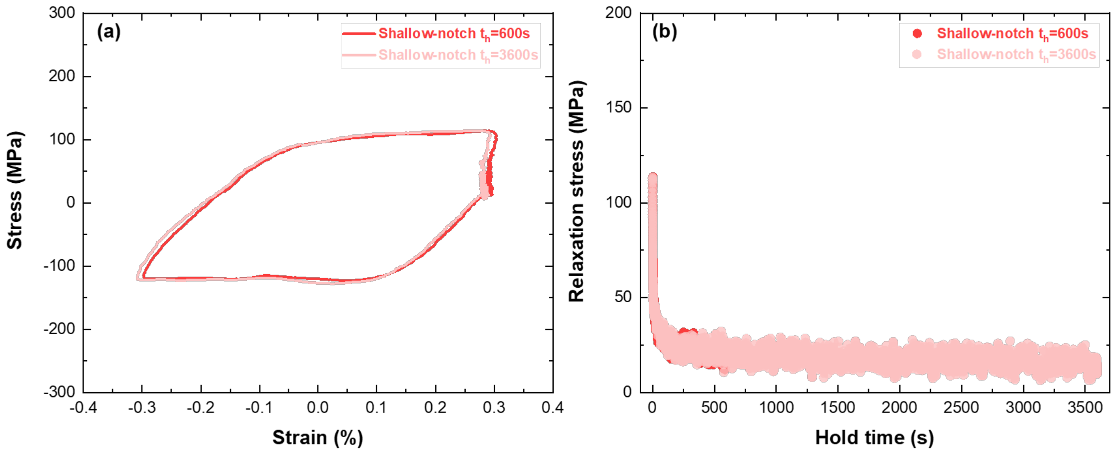

Figure 17. Comparison of average global stress vs nominal strain hysteresis loops and average global stress relaxation curves of the cycle 10 of shallow-notch specimens with 600 s and 3600 s hold time at 950°C.

5.2 NUMERICAL ANALYSIS

Figure 18 presents the finite element model for smooth bar, V-notch and shallow-notch specimens. The element type used is a four-node bilinear brick element (CAX4 in ABAQUS), and the mesh near notch root and notch boundaries is refined.

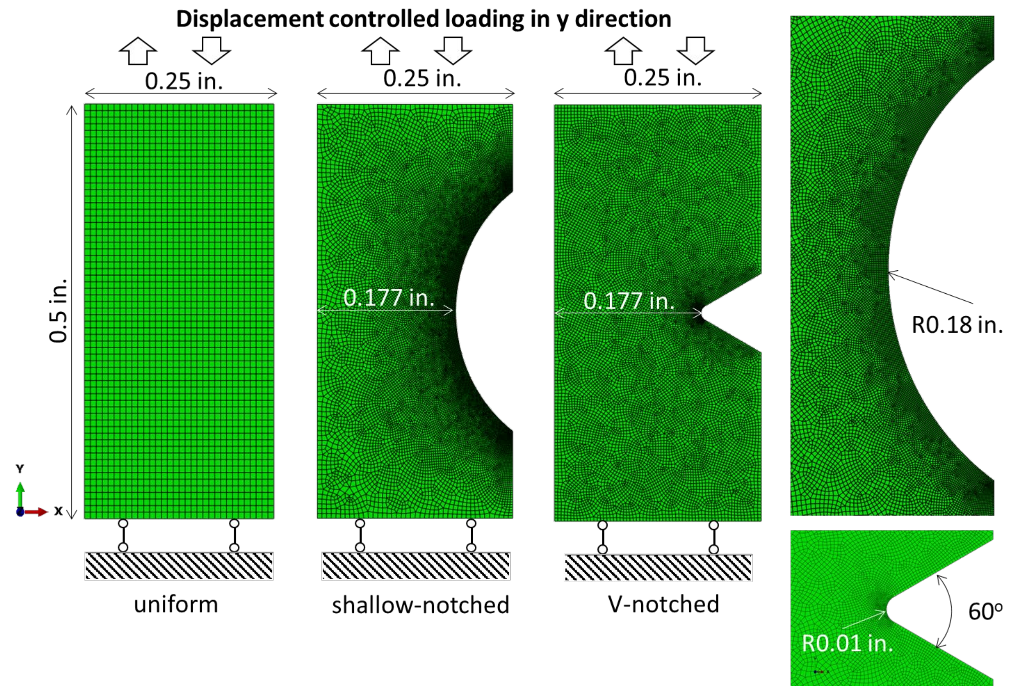

Figure 18. Finite element model for smooth bar, V-notch and shallow-notch specimens.

Figure 19 shows the comparison of the stress relaxation curve and the normalized stress relaxation curve from numerical results at the 3rd cycle in standard uniform specimen, shallow-notch specimen, and V-notch specimen. Consistent with experimental results, the notch specimens show comparable stress relaxation behavior as the uniform specimens.

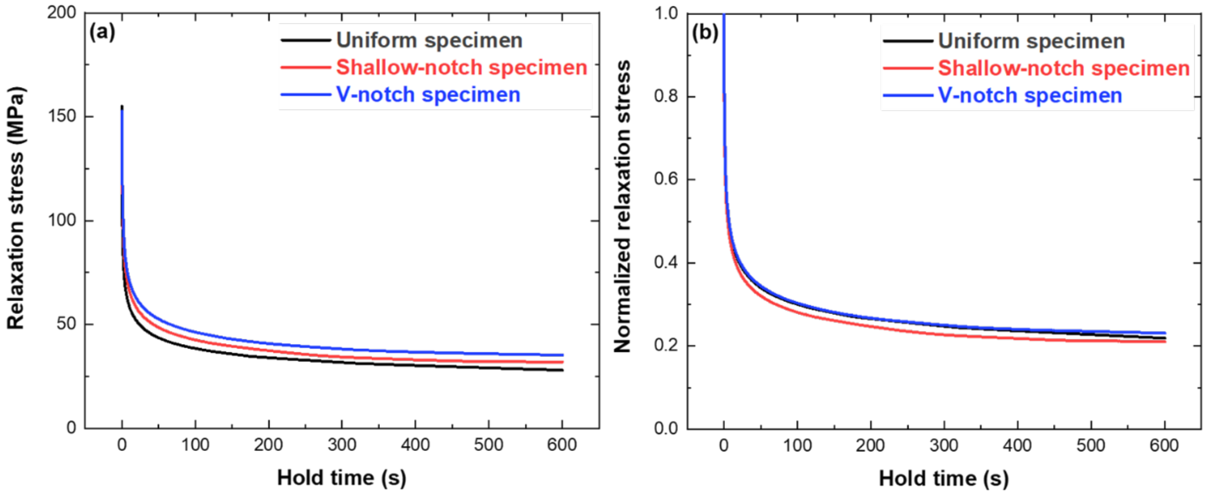

Figure 19. Numerical modeling results on the stress relaxation curves and normalized stress relaxation curves of the third applied cycle for the notch specimens and the smooth bar specimen at 950 °C.

To investigate the multiaxial stress effect, the stress triaxiality factor, TF, contours of the 3rd cycle are calculated according to Eq. 23 and are presented at the loading right before the holding and at the end of the holding period in Figure 20. According to finite element modeling (FE) results, the stress triaxiality factor does not change significantly during the hold. The maximum TFs in the V-notch specimen and shallow-notch specimen are about 1.5 and 1.0, respectively.

$$\mathrm{TF} = \frac{\frac{1}{3}\sigma_{ii}}{\sqrt{\frac{3}{2}S_{ij}S_{ij}}} \tag{23}$$

where σ_{ii} is the principal stress component and S_{ij} is the deviatoric stress.

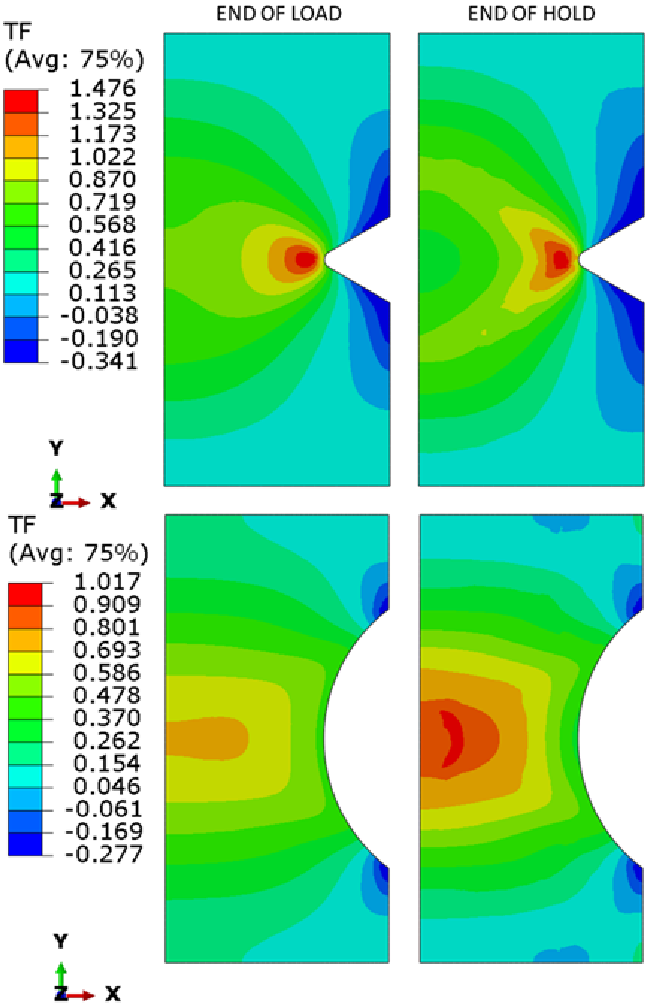

Figure 20. Stress triaxiality factor contours of the 3rd cycle at the beginning of the holding and at the end of the holding period.

Figure 21 shows the contours of the maximum equivalent strain range of uniform and notch specimens calculated per the procedure in ASME Section III, Division 5, HBB-T-1413. The maximum equivalent strain range of the V-notch specimen and shallow-notch specimen are located at the root of the notch. The equivalent strain range will be used for the analysis and development of multiaxial CF life curve at temperature of 950°C.

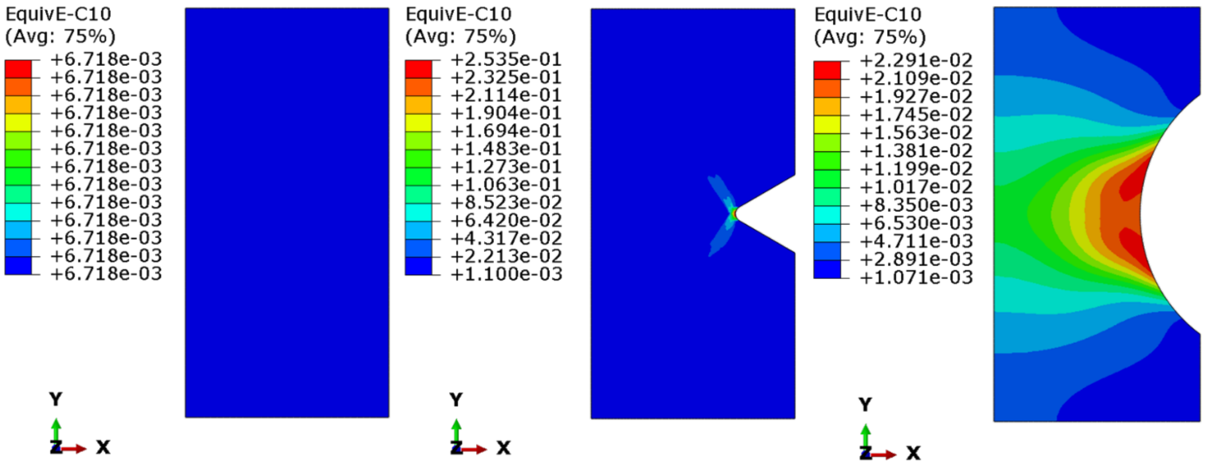

Figure 21. Equivalent strain range contour of uniform specimen and notch specimens.

The contours of the inelastic strain rate at the initial 10 s hold of the 3rd cycle of uniform and notch specimens are presented in Figure 22. The numerical results illustrated the effect of the notches on the changes in inelastic deformation rate. V-notch and shallow-notch specimens show 2 to 3 times higher inelastic strain rate than the value of the standard uniform specimen.

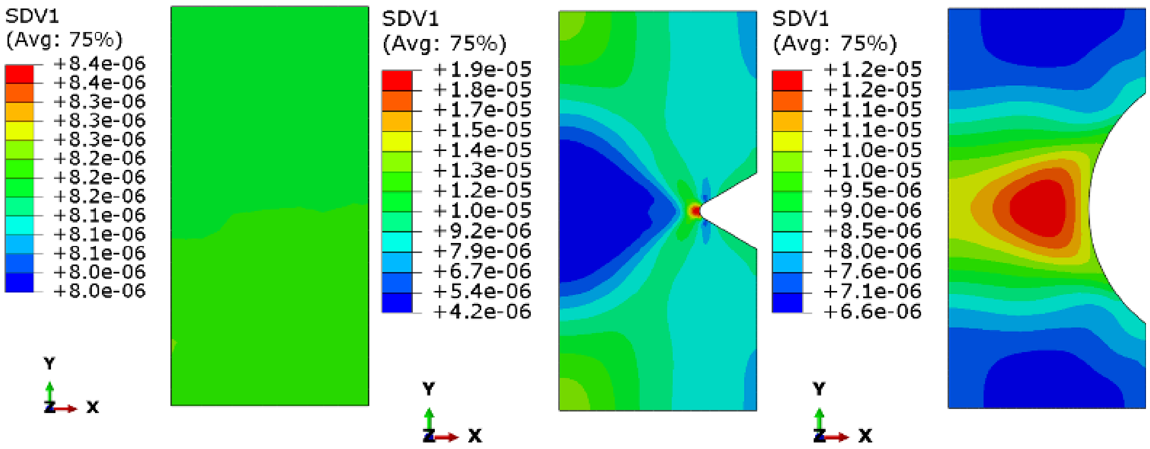

Figure 22. Contours of the inelastic strain rate at the initial 10 s hold of the 3rd cycle of uniform and notch specimens.

To investigate the geometric effect on elastic follow-up factor and study the effect of elastic follow-up on stress relaxation behavior in this study, the elastic follow-up factors were calculated using the numerical models. A schematic of the stress strain curve of tensile-hold CF test illustrating definition of elastic follow-up factor and the mixed stress-strain-controlled mode is presented in Figure 23. The elastic follow-up factor, q, is generally defined as a ratio of the strain with increased inelastic strain $\Delta\epsilon_{\text{in}}$ to the elastic strain

$\Delta\epsilon_e$during hold-time period under a uniaxial loading condition, given by Eq. 24, and schematically shown in Figure 23.

$$q = \frac{|AC|}{|AB|} = -\frac{\Delta\epsilon_{in}}{\Delta\epsilon_e} \tag{24}$$

where $\Delta\epsilon_{in}$ is the increase in inelastic strain during the hold and $\Delta\epsilon_e$ is the decrease in elastic strain during the hold.

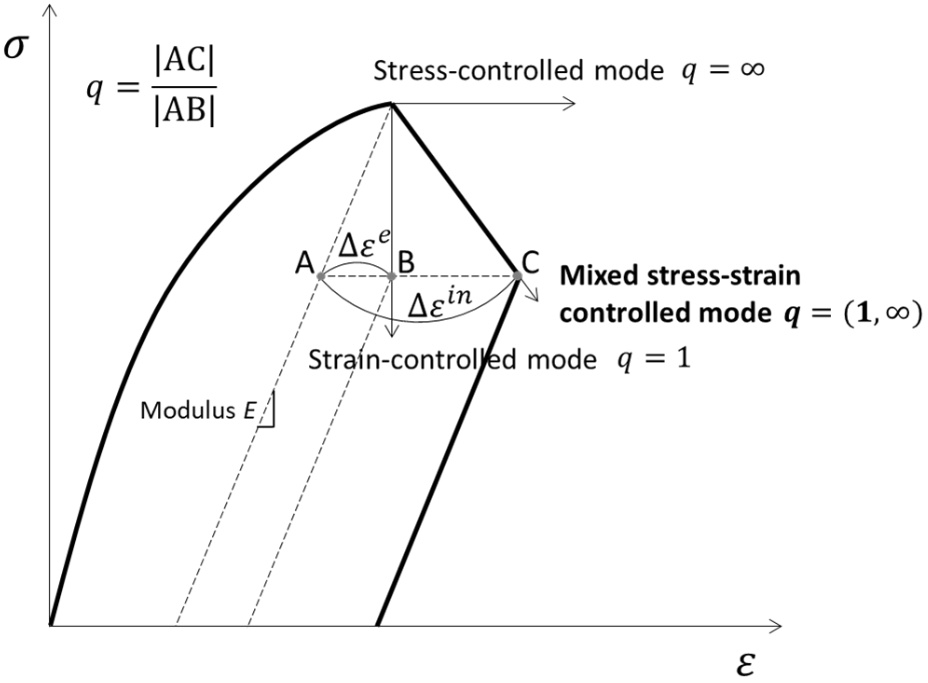

Figure 23. Schematic of the definition of elastic follow-up factor under uniaxial stress state.

Compared with the strain-controlled mode (i.e., elastic follow-up factor $q = 1.0$) for the uniaxial uniform specimens, discontinuous geometric shapes of notch specimens always induce a mixed stress-strain-controlled mode. In this case, the elastic follow-up phenomenon contributes to the decrease in stress relaxation rate during hold time and hence an enhanced creep damage in the structural component. In the multiaxial stress state, the elastic follow-up factor can be calculated using Eq. 25 (Messner, M. C. et al. 2019):

$$q = -\frac{\Delta W_{in}}{\Delta W_e} \tag{25}$$

where ΔW_{in} is the changes in inelastic strain energy and ΔW_e is changes in elastic strain energy at holding period. Moreover, the magnitude of time interval in Eq. 25 reveals a difference between a tangent and a secant definition of the elastic follow-up for a structural component. In the current study, the elastic follow-up factor was calculated in each element based on Eq. 25. In the current study, the near-tangent values of elastic follow-up are calculated using data of the initial 10 s during the holding.

Figure 24 shows the contours of elastic follow-up factor of standard uniform, shallow-notch, and V-notch specimens of 0.5 in. and 0.75 in. gauge sections. This result quantitatively illustrates the geometric effect on elastic follow-up factor. The elastic follow-up factor in both 0.5 in. and 0.75 in. gauge-length cases for the standard uniform specimen was distributed uniformly and equals to 1.0 regardless of specimen dimension. For the notch specimens, changes in the contours of elastic follow-up factor were observed when the simulated gauge length increases from 0.5 in., in Figure 24b and c, to 0.75 in., in Figure 24e and Figure 24f. As the gauge length of specimen increases, the distribution of elastic follow-up factor around the notch area changes. An elastic follow-up factor of as high as 1.5, is induced around the notch area. It is noted that the locations with the largest elastic follow up are strongly dependent on the geometric shape and the effective length of the notch specimens, which, in turn affect stress-relaxation rate.

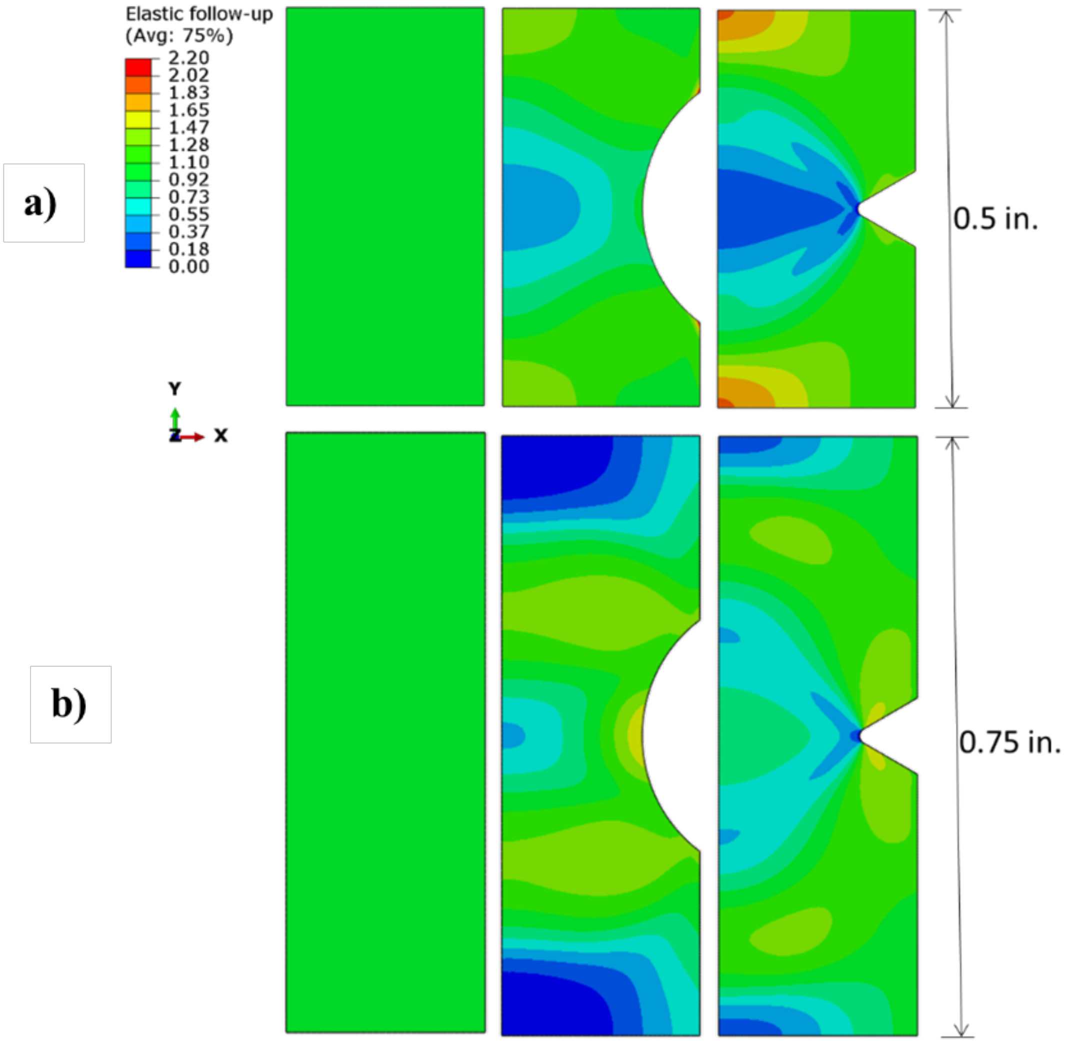

Figure 24. Contours of the average elastic follow-up factor q from the initial 10 s of the hold time at 10th cycle for the three specimens with (a) 0.5 in. gauge length and (b) 0.75 in. gauge length specimens.

As described above, notches in the test article introduce the multiaxial stress state and elastic follow-up, which in turn, as expected, would influence the relaxation behavior during the hold period. To illustrate the multi-axial stress state and elastic follow-up effects on stress relaxation behavior, Figure 25 shows the normalized stress relaxation curves with given stress triaxiality factor and elastic follow-up factor collected from FE results. The TF in this plot are the values at the beginning of the tensile hold. Note that the case of

TF=0.333 and q=1.0 represents the standard uniform specimen under uniaxial loading condition. As shown in Figure 25, it is likely that both triaxiality factor and follow-up factor plays roles in the increase of stress relaxation rate, despite insignificantly.

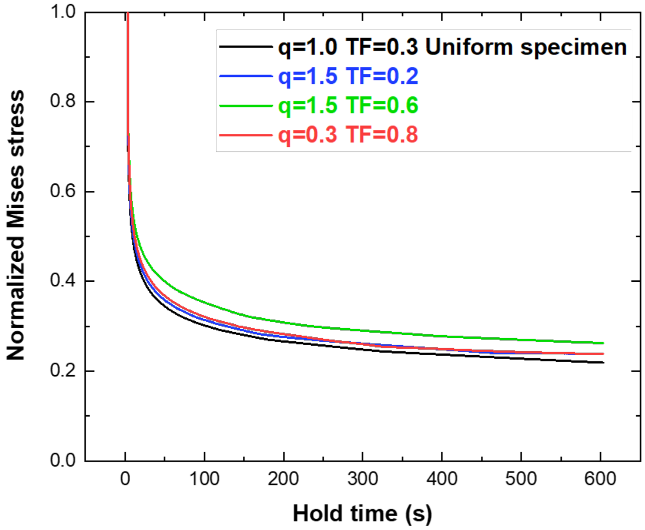

Figure 25. Examples of the normalized stress relaxation curves at the 3rd cycle at locations with different given stress triaxiality factor and elastic follow-up factor.

The experimental CF data on notch specimens with tensile hold times of 600 s and 3,600 s are summarized in Figure 26 using the numerical calculated maximum equivalent strain ranges, along with data on the standard smooth bar CF specimens. The best fit CF curves for tensile hold time for Alloy 617 at 950°C and the developed CF life curves (i.e., the CF curves shown in Figure 11) are also plotted as a comparison. The results show that the developed CF life curves are conservative.

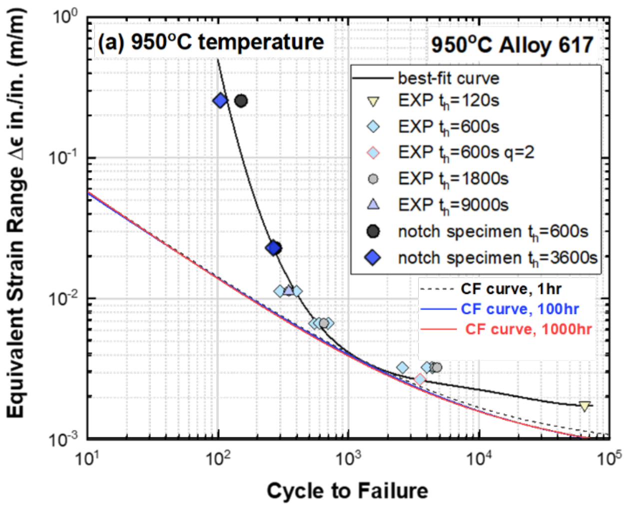

Figure 26. Tensile-hold creep-fatigue experimental data for alloy 617 at 950°C on notch specimens and standard smooth bar specimens.

6. SUMMARY

In this report, the standard uniaxial creep-fatigue data of Alloy 617 at temperatures of 950°C and 850°C were analyzed using energy-based method in support of the development of creep-fatigue design curves. The mechanical responses of Alloy 617 were simulated using a unified viscoplastic constitutive model, and the numerical data were then used to collect key information for extrapolation of the creep-fatigue life cycles to long hold times and low strain ranges. The parameters in this constitutive model were re-calibrated using the experimental creep-fatigue data at temperatures of 950°C and 850°C in this work. Due to the absence of creep-fatigue experimental data at 800°C, the isochronous curves in Alloy 617 Code Case N-898 were used to develop the constitutive model parameters at 800°C. Based on this extrapolation method and the creep-fatigue failure criteria, the preliminary creep-fatigue life curves with tensile hold times of 1 hr, 100 hr, and 1000 hr were developed at temperatures of 950°C, 850°C, and 800°C for Alloy 617.

In addition, experimental creep-fatigue tests on two types of notch specimens were designed and conducted at temperature of 950°C to investigate the role of notch geometry on the stress relaxation behavior and creep-fatigue life. A unified viscoplasticity model was implemented into finite element simulation through a user defined material subroutine in ABAQUS to investigate the multiaxial stress relaxation and elastic follow-up effect on the effectiveness of notch geometries in resisting the stress relaxation. The creep-fatigue life was reduced in notch specimens in comparison to standard uniform specimens at same global loading condition, but the effect of tensile hold times on the creep-fatigue failure cycles in notch specimens is not significant. In comparison to the standard uniform specimens, notch specimens exhibit similar average global relaxation stresses, but with much larger maximum strain ranges due to the notches. The results on creep fatigue of the notch specimens show that the developed creep-fatigue life curves are conservative.

REFERENCE

ASMT E2714-13, “Standard Test Method for Creep-Fatigue Testing”, ASTM International, West Conshohocken, PA.

ASTM-E606-21, “Standard Test Method for Strain-Controlled Fatigue Testing”, ASTM International, West Conshohocken, PA.

ASTM E292-09, “Conducting Time-for-Rupture Notch Tension Tests of Materials”, ASTM International, West Conshohocken, PA.

Barua, B, Messner, M.C., Sham, T.-L., Jetter, R. I., Wang, Y., (2020), "Preliminary description of a new creep-fatigue design method that reduces over conservatism and simplifies the high temperature design process", ANL-ART-194, Argonne National Laboratory, Lemont, IL.

Barua, B, Messner, M.C., Wang, Y., Sham, T.-L., Jetter, R. I. (2021), "Draft Rules for Alloy 617 Creep-Fatigue Design using an EPP+SMT Approach", ANL-ART-227, Argonne National Laboratory, Lemont, IL

Code Case N-898 (2019), ASME BPVC Code Case for Use of Alloy 617 (UNS N06617) for Class A Elevated Temperature Service Construction Section III, Division 5.

Hou, P, Wang, Y. and Sham, T.-L. (2023a), “A Method for Evaluation of Creep-Fatigue Life at Low Strain Ranges”, Proceedings of the ASME 2023 Pressure Vessels and Piping Conference, PVP2023-106512, American Society of Mechanical Engineers, Atlanta, Georgia.

Hou, P, Wang, Y. and Sham, T.-L. (2023b), “Notch Effect On Creep-Fatigue Behavior Of Alloy 617 At Elevated Temperature” Proceedings of the ASME 2023 Pressure Vessels and Piping Conference, PVP2023-106503, American Society of Mechanical Engineers, Atlanta, Georgia.

Messner, M. C., Sham, T. L., Wang, Y., and R. I. Jetter, R.I. (2018), “Evaluation of methods to determine strain ranges for use in SMT design curves”, ANL-ART-138, Argonne National Laboratory, Lemont, IL.

Messner, M.C. (2022). ASME Code Revisions to Incorporate 316H and Alloy 617 Viscoplastic Constitutive Models to Section III, Division 5 and Code Case N-898 (No. ANL-ART-249). Argonne National Lab.(ANL), Argonne, IL (United States).

Messner, M.C. and Sham, T.L. (2021). A Viscoplastic Model for Alloy 617 for Use With the ASME Section III, Division 5 Design by Inelastic Analysis Rules. In Pressure Vessels and Piping Conference (Vol. 85314, p. V001T01A034). American Society of Mechanical Engineers.

Messner, M. C., Jetter. B, and Sham, T. L. (2019), “A Method for Directly Assessing Elastic Follow Up in 3D Finite Element Calculations,” Proceedings of the ASME 2019 Pressure Vessels & Piping Conference, PVP2019-93644, American Society of Mechanical Engineers, New York.

Wang, Y., Jetter, R. I., Krishnan, K., and Sham, T.-L (2013) “Progress Report on Creep-Fatigue Design Method Development Based on SMT Approach for Alloy 617”, ORNL/TM-2013/349, Oak Ridge National Laboratory, Oak Ridge, TN.

Wang, Y., Jetter, R. I. and Sham, T.-L (2014), “Application of Combined Sustained and Cyclic Loading Test Results to Alloy 617 Elevated Temperature Design Criteria”, ORNL/TM-2014/294, Oak Ridge National Laboratory, Oak Ridge, TN.

Wang, Y., Jetter, R. I., Baird, S. T., Pu, C. and Sham, T.-L. (2015), “Report on FY15 Two-Bar Thermal Ratcheting Test Results”, ORNL/TM-2015/284, Oak Ridge National Laboratory, Oak Ridge, TN.

Wang, Y., Jetter, R. I., and Sham, T.-L. (2016a), "FY16 Progress Report on Test Results In Support Of Integrated EPP and SMT Design Methods Development" ORNL/TM-2016/330, Oak Ridge National Laboratory, Oak Ridge, TN.

Wang, Y., Jetter, R. I., and Sham, T.-L. (2016b), "Preliminary Test Results in Support of Integrated EPP and SMT Design Methods Development", ORNL/TM-2016/76, Oak Ridge National Laboratory, Oak Ridge, TN.

Wang, Y., Jetter, R.I., and Sham, T.-L. (2017a), "Report on FY17 Testing in Support of Integrated EPP-SMT Design Methods Development", ORNL/TM-2017/351, Oak Ridge National Laboratory, Oak Ridge, TN.

Wang, Y., Jetter, and Sham, T.-L. (2017b), "Pressurized Creep-Fatigue Testing of Alloy 617 Using Simplified Model Test Method", Proceedings of the ASME 2017 Pressure Vessels and Piping Conference, PVP2017-65457, American Society of Mechanical Engineers, New York, NY.

Wang, Y., Jetter, R. I., Messner, M., Mohanty, S., and Sham, T.-L. (2017c), "Combined Load and Displacement Controlled Testing to Support Development of Simplified Component Design Rules for Elevated Temperature Service", Proceedings of the ASME 2017 Pressure Vessels and Piping Conference, PVP2017-65455, American Society of Mechanical Engineers, New York, NY.

Wang, Y., Jetter, R. I., Messner, M., and Sham, T.-L. (2018), "Report on FY18 Testing Results in Support of Integrated EPP-SMT Design Methods Development", ORNL/TM-2018/887, Oak Ridge National Laboratory, Oak Ridge, TN.

Wang, Y., Jetter, R. I., Messner, M., and Sham, T.-L. (2019), "Development of Simplified Model Test Method for Creep-fatigue Evaluation", Proceedings of the ASME 2019 Pressure Vessels and Piping Conference, PVP2019-93648, American Society of Mechanical Engineers, New York, NY.

Wang, Y., Hou, P., Jetter, R. I., and Sham, T.-L. (2020), "Report on FY2020 Test Results in Support of the Development of EPP Plus SMT Design Method", ORNL/TM-2020/1620, Oak Ridge National Laboratory, Oak Ridge, TN.

Wang, Y., Hou, P., Jetter, R. I., and Sham, T.-L. (2021a), "Evaluation of the Primary-Load Effects on Creep-Fatigue Life of Alloy 617 Using Simplified Model Test Method", Proceedings of the ASME 2021 Pressure Vessels and Piping Conference, PVP2021-61658, American Society of Mechanical Engineers, New York, NY

Wang, Y., Hou, P., Jetter, R. I., and Sham, T.-L. (2021b), "Report on FY2021 Test Results in Support of the Development of EPP Plus SMT Design Method", ORNL/TM-2021/2159, Oak Ridge National Laboratory, Oak Ridge, TN.

Wright, R. N. (2021). "Draft ASME Boiler and Pressure Vessel Code Cases and Technical Bases for Use of Alloy 617 for Construction of Nuclear Components Under Section Ill, Division 5". INL/EXT-15-36305, Idaho National Laboratory, Idaho Falls, Idaho.